RSC Advances

PAPER

View Article Online
View Journal | View Issue

Cite this: *RSC Adv.*, 2022, **12**, 11534

A multi-color persistent luminescent phosphor β-$NaYF_4$:RE^{3+} (RE = Sm, Tb, Dy, Pr) for dynamic anti-counterfeiting†

Bohan Wang,[a] Zhihao Wang,*[b] Peng Mao [a] and Yu Wang *[a]

Received 3rd March 2022
Accepted 7th April 2022

DOI: 10.1039/d2ra01425d

rsc.li/rsc-advances

Conventional luminescent materials generally exhibit uni-color and transient emission under UV excitation, which makes them mediocre in the field of anti-counterfeiting. The high-level anti-counterfeiting techniques are always becoming more complicated and in need of multi-color and persistent luminescent materials. Herein, we report a series of β-$NaYF_4$:RE^{3+} (RE = Sm, Tb, Dy, Pr) persistent luminescent phosphors with multi-color emitting and ultra-long persistent luminescence under the irradiation of X-rays. The effects of doping concentrations of RE^{3+} on the size, morphology, radioluminescence and afterglow performance of the products are investigated in detail. Hexagonal structured rod-like β-$NaYF_4$:Tb^{3+} crystals show super strong X-ray response and the afterglow signal lasts for up to seven days after X-rays are turned off. Upon X-rays irradiation, some of the F^- ions are expected to escape from the crystal lattice by elastic collisions, leading to the generation of Frenkel defects: the F vacancies ($V_F^{\bullet}$) and interstitials ($F_i^{'}$), which capture electrons and release them slowly to achieve different afterglow emission times. Taking advantages of the extraordinary radioluminescence performance of the β-$NaYF_4$:RE^{3+} persistent luminescent phosphors, the dynamic anti-counterfeiting patterns that containing rich time-resolved information were successfully designed.

Introduction

Anti-counterfeiting technology is closely related to information and data security. How to effectively prevent counterfeiting has been a huge challenge and has received worldwide attention for a long time.[1–3] Traditional luminescent materials generally present uni-color emission upon ultraviolet (UV) and near-infrared (NIR) light excitation. Based on this, the most common and traditional anti-counterfeiting luminescence achieved by the sole-mode down/up converting luminescence has been frequently witnessed in terms of banknotes, invoices, and commodities. However, owing to the fact that the labels based on traditional luminescent materials are easy to imitate, the anti-counterfeiting efficiency based on a sole luminescence mode is far from meeting the requirements of practical applications to guarantee a high level of data and information safety.[4–7] To address this deficiency, developing more complicated anti-counterfeiting techniques by increasing the luminescent modes and changing the excitation source has become a quite challenging topic. It is worth mentioning that X-rays excited materials, also referred to as scintillators, are of great interest in the fields of X-rays detectors, lasing, imaging, *etc.*[8] On the basis that X-rays show deeper penetration depth and higher excitation energy with respect to UV and NIR, the anti-counterfeiting labels made of X-rays excited materials may present novel luminescence behavior and may open a new door for anti-counterfeiting technology. Very recently, the label fabricated by Yb^{3+}/Er^{3+}/Bi^{3+} doped $Cs_2Ag_{0.6}Na_{0.4}InCl_6$ material is evidenced to be promising in high-security anti-counterfeiting since the material exhibits different luminescence behaviors under specific excitation, such as X-rays, UV, and NIR sources.[9]

Persistent luminescent phosphors (PLPs) are a kind of eco-friendly energy storage material that possesses the attractive nature of absorbing and storing energy from an excitation source and emitting light for a long time after the excitation ends. The release time of afterglow varies from several seconds to even several days depending on the luminescence matrix and additive.[10,11] A great number of novel persistent phosphors, such as $SrAl_2O_4$:Eu^{2+}/Dy^{3+}, $ZnGa_2O_4$:Cr^{3+} and CaS:Eu^{3+}/Ce^{3+}, have been fabricated and used in targeted tumor PL imaging, multi-model imaging, bio-sensing, and even new energy source exploration.[12–15] However, due to the intrinsic shortcomings of solid-state method, these materials are generally coarse particles with obvious aggregation appearance, leading to the lowered luminous efficiency and limited development prospects.[16]

[a]*International Collaborative Laboratory of 2D Materials for Optoelectronics Science and Technology of Ministry of Education, Institute of Microscale Optoelectronics, Shenzhen University, Shenzhen 518060, China. E-mail: wangyu@szu.edu.cn*

[b]*Research and Develop Center, Shenzhen Huake Chuangzhi Technology Co., Ltd., Shenzhen, 518116, China. E-mail: wang.zhihao@huake-tek.com*

† Electronic supplementary information (ESI) available. See https://doi.org/10.1039/d2ra01425d

Comparatively, fluorides, which are readily synthesized by wet-chemical methods, generally present narrow size distribution and favorable morphology uniformity. As an excellent luminescent host material, β-$NaYF_4$ may reduce the quenching of the excited states of lanthanide ions due to its low phonon energy.[17–19] In addition, the chemical bond between lanthanide ions and fluorine ions is mainly ionic, and the wide band gap enables good transparency in the visible and ultraviolet range. The two factors make β-$NaYF_4$ an excellent carrier of luminescent substance.[20,21] Recently, literature have reported that β-$NaYF_4$:Tb^{3+} generates long afterglow under the excitation of X-rays, and this characteristic endow β-$NaYF_4$:Tb^{3+} with great application potential in the fields of flat panel X-rays detectors and photodynamic therapy.[22,23] Nevertheless, the studies of the β-$NaYF_4$ based PLPs on multi-color dynamic anti-counterfeiting materials, to the best of our knowledge, are still rare.

In this work, the β-$NaYF_4$:RE^{3+} (RE = Sm, Tb, Dy, Pr) PLPs with long afterglow and multi-color emission under X-rays excitation have been synthesized by a facile hydrothermal method. The morphology evolution after RE^{3+} incorporation is systematically investigated. Moreover, the radioluminescence (RL) behaviors and afterglow mechanisms of the products are deciphered. It is worthy highlight that, after turning off the excitation source, an afterglow signal lasts up to seven days can be detected. Benefit from the excellent afterglow performances, the application of the as-produced PLPs in dynamic multi-color anti-counterfeiting was successfully performed. We believe that our initiative on the β-$NaYF_4$:RE^{3+} based dynamic luminescent anti-counterfeiting could arouse wide scientific and technological interests.

Results and discussion

Characterization of the β-$NaYF_4$:$x$$Tb^{3+}$ (x = 0.01–0.30) samples

Rietveld structure refinement pattern of the representative x = 0.10 sample was carried out by using the crystallographic data of standard β-$NaYF_4$ (JCPDS card no. 16-0334) as initial structure model,[24,25] and the results are presented in Fig. 1a. The refinement is stable and ended with low R-factors, indicating that the Tb^{3+} doped β-$NaYF_4$ with pure phase can be hydrothermally obtained. XRD patterns of all the $NaYF_4$:$x$$Tb^{3+}$ (x = 0.01–0.30) samples are compared in Fig. 1b, from which it is seen that the characteristic diffraction intensities and positions can all be well indexed as β-$NaYF_4$ in each case. Owing to the identical electric charge and similar ionic radii of Y^{3+} and Tb^{3+}, the position of Y^{3+} can be easily replaced by Tb^{3+} in the β-$NaYF_4$ crystals. It is worth mentioning that the diffraction peak shifts slightly towards the lower angle side (Fig. 1b) owing to the substitution of smaller Y^{3+} ($r_{Y^{3+}}$ = 1.159 Å) by the relatively larger Tb^{3+} ($r_{Tb^{3+}}$ = 1.180 Å). The details of lattice parameters a/b (a = b), c and lattice volume V of these samples obtained by Rietveld structure refinement are listed in Table S1,† from which a monotonically increasing tendency is discernible for each case. The XRD patterns also indicate that there are some differences in relative intensities based on (110) and (101), suggesting a preferential crystallographic orientation of the samples.

The structure of β-$NaYF_4$, as shown in Fig. 1c, displays a strong cation disorder.[26] There are three types of cation occupation sites: (1a), (1f), and (2h). The nine F^- coordinated Y^{3+} ions occupy all the (1a) sites along with half of the (1f) sites. Meanwhile, Na^+ occupies the other half of the (1f) sites and half of the (2h) sites.[27] Various dopants can be facilely integrated into the β-$NaYF_4$ lattice through replacing these Y^{3+} sites.[28–30] The longer bond distance of Na^+-F^- than RE^{3+}-F^- at the (1f) site reduces the actual symmetry of the (1a) sites. As a consequence, the six capping F^- ions move up and down around the Y atom. These movements are unequal in a vast scale, yielding symmetry deterioration and leading to the high anisotropy of the hexagonal $NaYF_4$ structure. This is also an important factor for the strong emission of β-$NaYF_4$ as the host material for RE^{3+} doping.[28]

The scanning electron microscopy (SEM) images (Fig. 2a) show that the as-prepared samples generally composed of rod-like particles with submicron sizes. It is interesting that the particle size does not shrink until the Tb^{3+} doping content reaches 30%, rather than change slowly as the doping concentration increases. It is known that the Gibbs free energy of $NaREF_4$ steady increases with decreased RE^{3+} radius.[31] Accordingly, the incorporation of Tb^{3+} into the reaction system facilitated the nucleation of the products, and this effect became evident when the Tb^{3+} concentration increased up to 30%. Elemental distribution patterns of the sample are shown in Fig. 2b, from which no obvious composition segregation can be observed, indicating that the Tb^{3+} ions were successfully introduced into the products *via* hydrothermal reaction.

Radioluminescence (RL) behavior of the β-$NaYF_4$:RE^{3+} (RE = Tb, Sm, Dy, Pr) samples

The RL properties of the as-prepared β-$NaYF_4$:$x$$Tb^{3+}$ were investigated under X-rays irradiation at room temperature. During the measurement, the powders were filled into the sample cell to form a flat exposed surface. The X-rays spot was directly irradiated on the powder with fixed incident angle of 45°, and the emitted signal with emergence angle of 45° was collected by a spectrograph (Fig. 3a). It is notable that the diameter of the exposed surface of the sample is 1 cm, and X-rays spot completely covered the sample surface in each run of the measurement, which ensured the stability and comparability of the spectral data. Fig. 3b shows the variation in RL intensity of β-$NaYF_4$:Tb^{3+} with increasing Tb^{3+} contents. All the emission spectra present four typical Tb^{3+} emission bands centered at 489 nm ($^5D_4 \rightarrow {}^7F_6$), 546 nm ($^5D_4 \rightarrow {}^7F_5$), 584 nm ($^5D_4 \rightarrow {}^7F_4$), and 620 nm ($^5D_4 \rightarrow {}^7F_3$), with the green ($^5D_4 \rightarrow {}^7F_5$) transition dominates the whole spectra. The RL intensity was remarkably enhanced by increasing the doping content of Tb^{3+} from 1% to 10%. However, further increase in Tb^{3+} concentration results in decrease of the RL intensity (the inset in Fig. 3a). The results demonstrate that concentration quenching of Tb^{3+} in the β-$NaYF_4$ matrix occurred at x = 0.10. Specifically, when the doping ratio is less than 10%, the

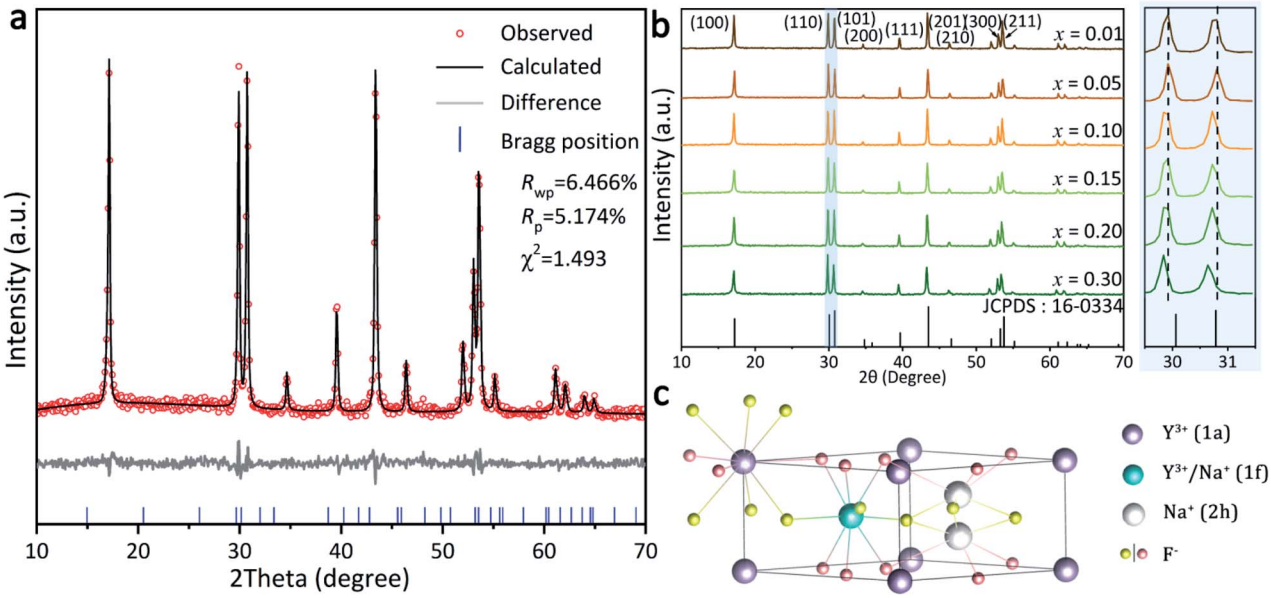

Fig. 1 (a) Shows Rietveld refinement patterns for the β-$NaYF_4$:Tb^{3+} samples, where R_{wp} represents the weighted profile reliability factor, R_p the pattern reliability factor and χ^2 the goodness of fitting. (b) XRD patterns of the as-synthesized β-$NaYF_4$:xTb^{3+} (x = 0.01–0.30) samples; (c) crystallographic structure of β-$NaYF_4$.

concentration of luminescence center rises with increasing Tb^{3+} incorporation, and the distance between Tb^{3+} ions is getting smaller, which would result in less energy loss in electron–hole pairs migration, leading to higher luminescence intensity. Further increasing Tb^{3+} concentration might cause self-quenching of Tb^{3+} activators, which is responsible for the decreased luminescence intensity at doping ratio between 10 and 30%.[32,33] Fig. 3c compares the emission spectra and decay curves of $NaYF_4$:0.10Tb^{3+} irradiated by UV (λ_{ex} = 378 nm) and X-rays. Despite that the emission spectra are similar, the persistent luminescence behavior was not observed upon UV excitation. Besides, RL peaks exhibit relatively higher signal-to-noise ratios, since the energy carried by the photons of X-rays was much higher than that of UV.

After switching off the X-rays source, these samples show prolonged RL decay with gradually decreasing intensity, suggesting the effective trapping ability of ionizing radiation. For instance, the residual emission of β-$NaYF_4$:0.10Tb^{3+} sample can still be directly observed by naked eyes after 24 h. We noted that the spectral profile of the afterglow does not change with

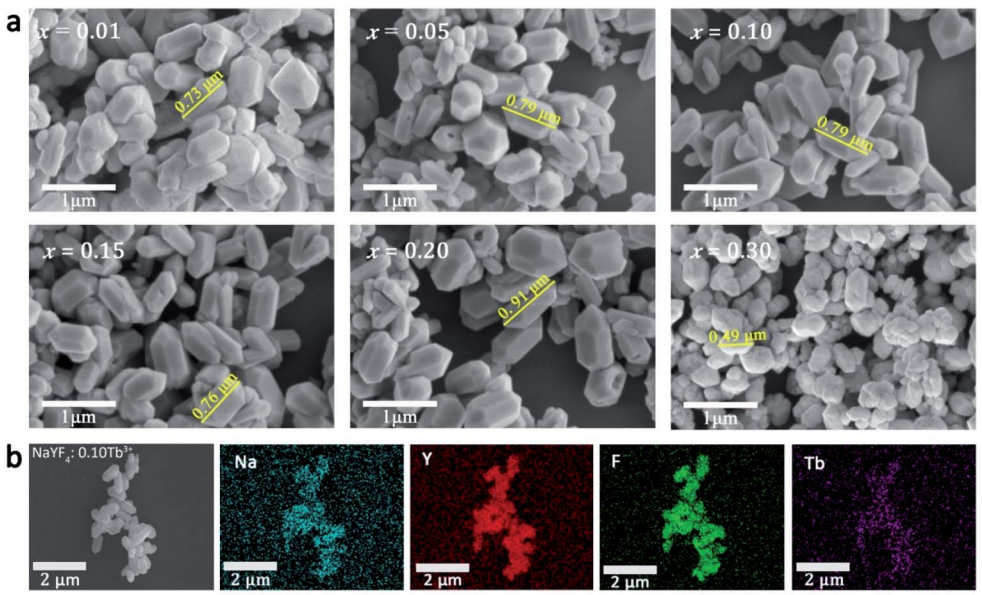

Fig. 2 (a) SEM images of the β-$NaYF_4$:xTb^{3+} (x = 0.01–0.30) samples; (b) EDS patterns of the representative β-$NaYF_4$:0.10Tb^{3+} sample.

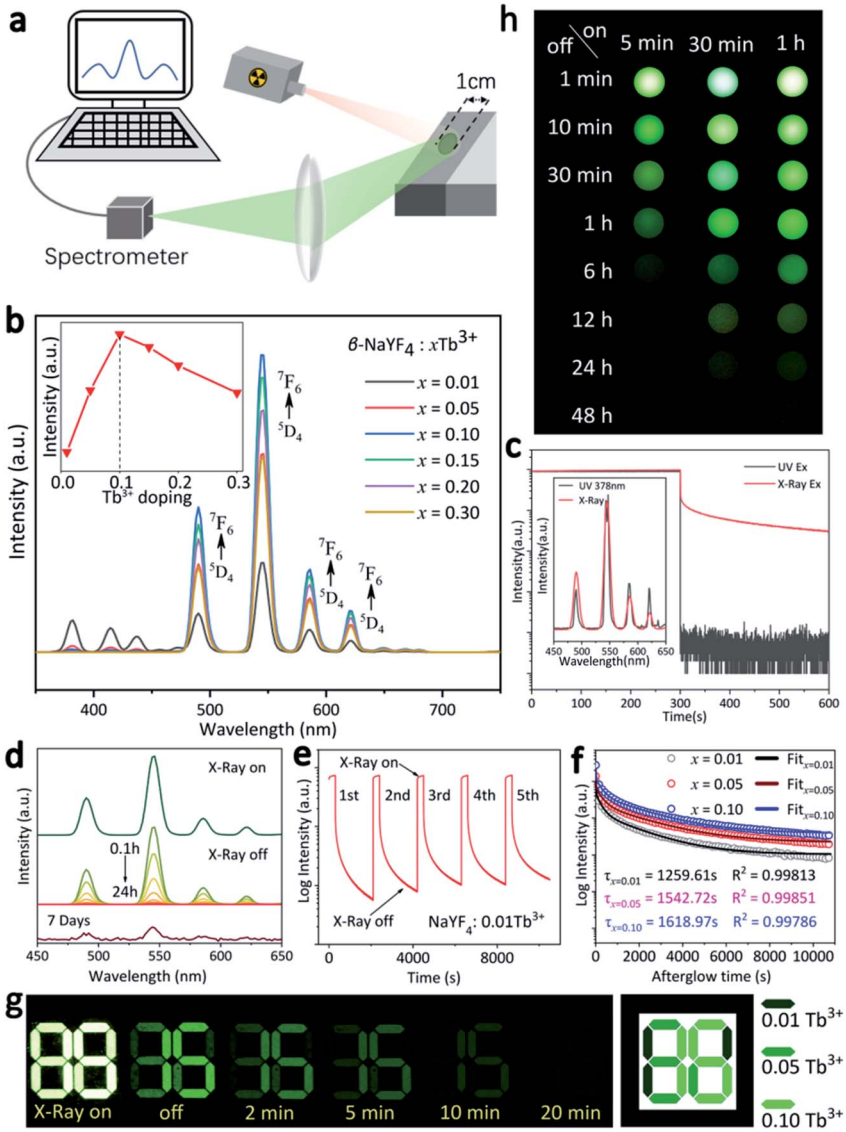

Fig. 3 (a) Schematic diagram of RL measurement; (b) RL of β-$NaYF_4$:xTb^{3+} (x = 0.01–0.30) under the excitation of X-rays at 50 kV; (c) the emission spectra and decay curves of $NaYF_4$:0.10Tb^{3+} irradiated by UV and X-rays; (d) RL spectra of β-$NaYF_4$:0.10Tb^{3+} recorded at 0.1–24 h and 7 days after 30 min of X-rays irradiation; (e) RL intensity of β-$NaYF_4$:0.10Tb^{3+} under repeated X-rays irradiation, with X-rays working 5 min and then suspending 30 min, and the cycle was repeated for 5 times; (f) afterglow intensity of $NaYF_4$:xTb^{3+} (x = 0.01, 0.05, 0.10), as a function of time after cessation of X-rays, all the samples were irradiated at 50 kV X-rays for 5 min; (g) the digital photos showing afterglow effects of the β-$NaYF_4$:xTb^{3+} (x = 0.01, 0.05, 0.10) samples; (h) images of the discs made by β-$NaYF_4$:0.10Tb^{3+} at different afterglow times (1 min to 48 h) after irradiation by 50 kV X-rays for 5 min, 30 min, and 1 h.

increasing decay time (Fig. 3d), indicating that the continuous emission arises from Tb^{3+}. It can also be verified from Fig. 3d that the afterglow signal of β-$NaYF_4$:0.10Tb^{3+} is still detectable even after 7 days. It is seen from Fig. 3e that the afterglow intensity is steady throughout the repetitious X-rays irradiation and cessation processes, confirming the high stability of the afterglow performance.

The afterglow intensity of the phosphors increases monotonously with the beam voltage and with Tb^{3+} concentration (below 10%), as can be observed from Fig. S1† and 3f, respectively. The β-$NaYF_4$:xTb^{3+} (x = 0.01, 0.05, 0.10) samples were analyzed to have the afterglow lengths of 1259.61, 1542.72, and 1618.97 s after 5 min of X-rays irradiation, respectively. According to the dopant concentration-dependent afterglow characteristic, an anti-counterfeiting pattern was designed (Fig. 3g), the side length of the square pattern is about 32 mm (Fig. S2†). It is shown that the three phosphors are indiscernible by naked eyes under X-rays excitation due to the strong green emission. However, different information gradually emerged from the pattern with prolonging time after X-rays cessation. Specifically, the pattern showed the number "88" in 0-2 minutes and then changed to "36" and "15" after 5 min and 10 min, respectively. Apparently, the number "36" is hidden in this changing process, and it can only be identified within

a specified period of time (5–10 min in this case). This phenomenon means that the pattern fabricated by the β-$NaYF_4$:$x$$Tb^{3+}$ PLPs contains multi-level information, and dynamic anti-counterfeiting can be achieved during the whole attenuation process. Additionally, extending X-rays irradiation time can significantly prolong the afterglow time and increase the afterglow intensity, which was confirmed by the digital SLR camera, as shown in Fig. 3h. It is also worth highlighting that even 5 minutes of X-rays irradiation on β-$NaYF_4$:0.10Tb^{3+} can give rise to more than 6 hours of continuous visible emission, coinciding well with the fitting results shown in Fig. 3f.

The persistence luminescence is known to arise from captured charge carriers in traps that are persistently released under thermostimulation.[34] Accordingly, thermoluminescence (TL) spectroscopy was applied to evaluate the density and depth of traps in the $NaYF_4$:RE^{3+} (RE = Sm, Dy, Pr, Tb) samples, and the results are shown in Fig. 4a. It is seen that the samples exhibit TL peaks with different intensities and positions. The temperature at which the intensity reaches a maximum (T_m) is proportional to the trap depth (E),[35] and a reasonable relationship between the two factors can be presented as follows:[36,37]

$$E = T_m/500 \quad (1)$$

The E values of $NaYF_4$:RE^{3+} (RE = Sm, Dy, Pr, Tb) phosphors are determined to be 0.692, 0.800, 0.924 and 0.724 eV, respectively. The mechanism of energy capture and release of the long-lived afterglow behavior has been illustrated in term of the β-$NaYF_4$:Tb^{3+} PLPs (Fig. 4b). X-rays energies are primarily absorbed by the Y atoms in the lattice to generate energetic electrons owing to the photoelectric effects. These electrons are excited from valence band (VB) to the free state of conductive band (CB) and simultaneously lead to the generation of holes at VB. Meanwhile, through elastic collisions between large-momentum X-rays photons and small F^- ions, some of the F^- ions are expected to escape from the crystal lattice, leading to the generation of a corresponding quantity of Frenkel defects: the F vacancies ($V_F^{\cdot}$) and interstitials (F_i').[22] The $V_F^{\cdot}$ and F_i' may serve as electron traps and hole traps, respectively, during the luminescence process. Displacements of F^- at short and long distances classify the $V_F^{\cdot}$ as transient shallow and long-lived deep trap states, respectively. Both the shallow and deep traps of $V_F^{\cdot}$ can trap the electrons located at the bottom of CB. The holes trapped by F_i' can migrate towards Tb^{3+} emitters to form hole Tb^{3+} centers, inducing the transformation of Tb^{3+} to stable Tb^{4+}.[38,39] Recombination of the electrons trapped in $V_F^{\cdot}$ and the holes bound by Tb^{3+} can directly happen, followed by non-radiatively transferring energy to Tb^{3+}. The electrons located at the ground state of Tb^{3+} are consequently activated to high energy states and then produce luminescence.[40,41]

Multi-colour RL from orange to purple was modulated by doping RE^{3+} (RE = Sm, Tb, Dy, Pr) in the hexagonal structured $NaYF_4$ matrix. Owing to the fact that the emission intensity of the phosphors mainly varies with RE^{3+} doping concentration (Fig. S3†), the samples of β-$NaYF_4$:0.01Sm^{3+}, β-$NaYF_4$:0.10Tb^{3+}, β-$NaYF_4$:0.10Dy^{3+}, and β-$NaYF_4$:0.01Pr^{3+} with the optimal RL were selected for further characterization. EDS patterns shown in Fig. S4† confirm that Sm^{3+}, Dy^{3+}, and Pr^{3+} ions were also successfully doped in β-$NaYF_4$, and XRD results indicate that the dopants did not interfere the phase purity (Fig. S5†). The RL spectra of β-$NaYF_4$:RE^{3+} (RE = Sm, Tb, Dy, Pr) are compared in Fig. 5a. For $NaYF_4$:Sm^{3+}, the RL spectrum shows the characteristic emission of Sm^{3+}: 562 nm ($^4G_{5/2} \rightarrow {}^6H_{5/2}$), 601 nm ($^4G_{5/2} \rightarrow {}^6H_{7/2}$), 645 nm ($^4G_{5/2} \rightarrow {}^6H_{9/2}$) and 700 nm ($^4G_{5/2} \rightarrow {}^6H_{11/2}$), with the orange emission ($^4G_{5/2} \rightarrow {}^6H_{7/2}$ transition) being the most significant.[40,42,43] For $NaYF_4$:Dy^{3+}, the blue (480 nm) and yellow (572 nm) emission bands are attributed to the ($^4F_{9/2} \rightarrow {}^6H_{15/2}$) and ($^4F_{9/2} \rightarrow {}^6H_{13/2}$) transitions of Dy^{3+}, respectively. It is observed that $NaYF_4$:Pr^{3+} shows characteristic purple emission upon X-rays irradiation, the multi-peaks are due to the f–f transitions of Pr^{3+}.[44] Specifically, the strongest blue emission at 492 nm is attributed to the $^3P_0 \rightarrow {}^3H_4$ transition and the red emission at 614 nm is ascribed to the $^3P_0 \rightarrow {}^3H_6$ transition.[45,46] As exhibited in the CIE diagram and digital photos in Fig. 5b, multi-color emissions can be easily realized by X-rays

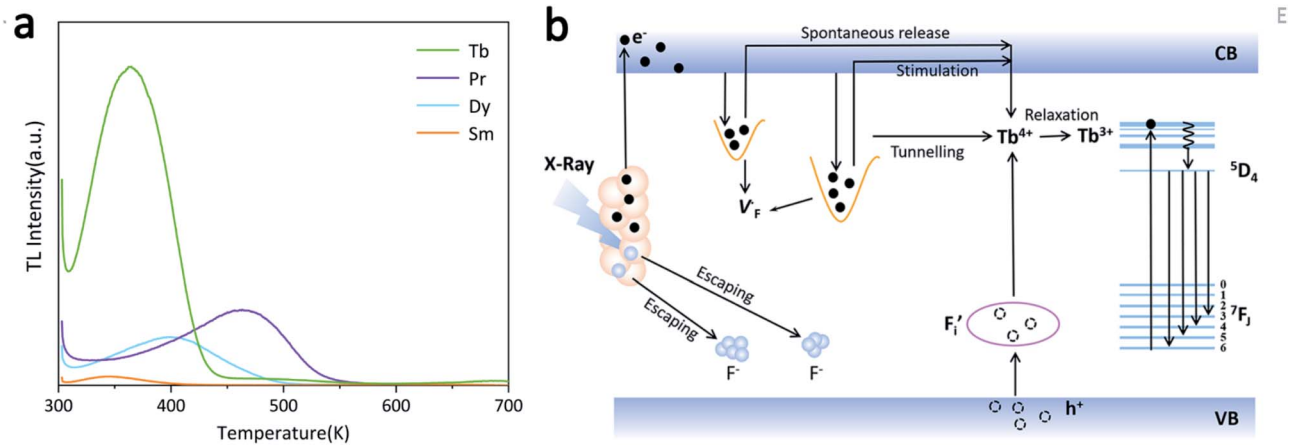

Fig. 4 (a) Thermoluminescence spectroscopy of $NaYF_4$:RE^{3+} (RE = Tb, Pr, Sm, Dy) samples; (b) proposed mechanism of the long-lived afterglow of $NaYF_4$:xTb^{3+} PLPs.

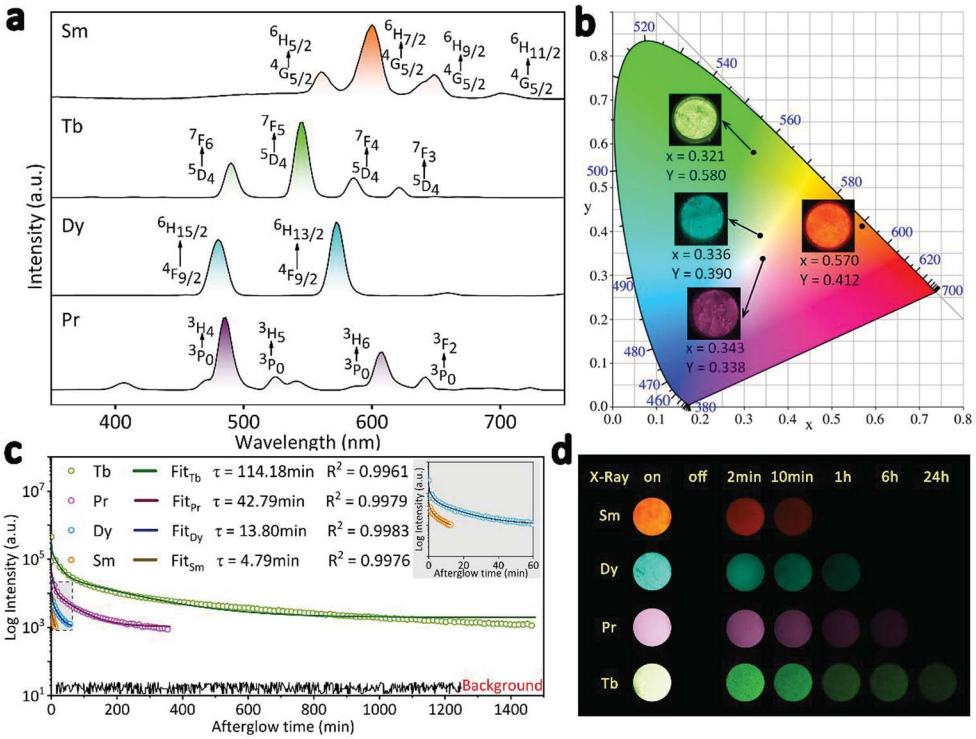

Fig. 5 (a) RL spectra of β-$NaYF_4$:0.01Sm^{3+}, β-$NaYF_4$:0.10Dy^{3+}, β-$NaYF_4$:0.01Pr^{3+}, and β-$NaYF_4$:0.10Tb^{3+} under the excitation of X-rays; (b) corresponding CIE coordinates and digital photos of the multi-color luminescence; (c) comparison of the afterglow decay curves of these β-$NaYF_4$:RE^{3+} PLPs, the decay curves were all obtained under X-rays irradiation at 50 kV for 30 min, and the monitoring wavelengths are 594, 573, 606 and 546 nm, respectively; (d) real time luminescence and afterglow appearances of these β-$NaYF_4$:RE^{3+} PLPs.

irradiating the β-$NaYF_4$:RE^{3+} samples. After switching off the X-rays source, all these samples present afterglow signal with gradually decreasing intensity (Fig. 5c). It is known that the duration of afterglow depends on the amount and depth of traps.[47] Since the multifarious energy levels of different rare earth ions can cause different numbers and depths of traps under X-rays radiation, the β-$NaYF_4$:RE^{3+} samples exhibited different lengths of afterglow. Fig. 5d gives the digital photos of the four samples after 30 min of X-rays irradiation. Corresponding to the decay curve, the afterglow appearances of all samples gradually fade away after irradiation. The afterglow of the orange β-$NaYF_4$:0.01Sm^{3+} and blue β-$NaYF_4$:0.10Dy^{3+} phosphors completely vanishes after 10 min and 1 h, respectively, while that of the purple β-$NaYF_4$:0.01Pr^{3+} and green β-$NaYF_4$:0.10Tb^{3+} phosphors can be observed by naked eyes for a much longer time.

Application of the $NaYF_4$:RE^{3+} phosphors in dynamic anti-counterfeiting

The UV-vis absorption spectra of the samples that used for fabricating anti-counterfeiting patterns are displayed in Fig. S6.† It is clearly that the absorption band of these samples distributes in the wide range of 200–800 nm, implying that the body color of these samples is white.[48] Taking advantages of the multi-color emitting and different afterglow features of the β-$NaYF_4$:RE^{3+} phosphors, three different patterns were designed for dynamic anti-counterfeiting. The fabrication process of the patterns is displayed in Fig. 6a. Fig. 6b exhibits the digital photos of the three designed patterns within a dynamic anti-counterfeiting process, and the original templates are shown in the right side. The "Wi-Fi" and grape patterns are about 21 mm in size, and the "Shenzhen University" pattern is about 31 mm in diameter (Fig. S2†). It is found that the patterns show different information at different time after X-rays irradiation. The image of "Wi-Fi" was composed of four bright parts under real time X-rays irradiation, whereas the curves disappeared in turn, and finally, became a single green dot after X-rays cessation. The whole process took about 10 minutes, and the brightness also gradually decreased. The same anti-counterfeiting principle reveals different information with the change of anti-counterfeiting pattern. Briefly, the fading process of a cluster of multi-color grapes is observable during the dynamic anti-counterfeiting process, and only the Chinese version of "Shenzhen University" is visible in the school badge in the final stage of the dynamic anti-counterfeiting process. It is notable that only the specific part of the information can be recognized at a particular time. Therefore, the anti-counterfeiting level is expected to reach a new height since more complex information can be stored through this strategy. This technique based on X-rays excited PLPs truly provides a new directional solution for the development of anti-counterfeiting labels with high efficacy.

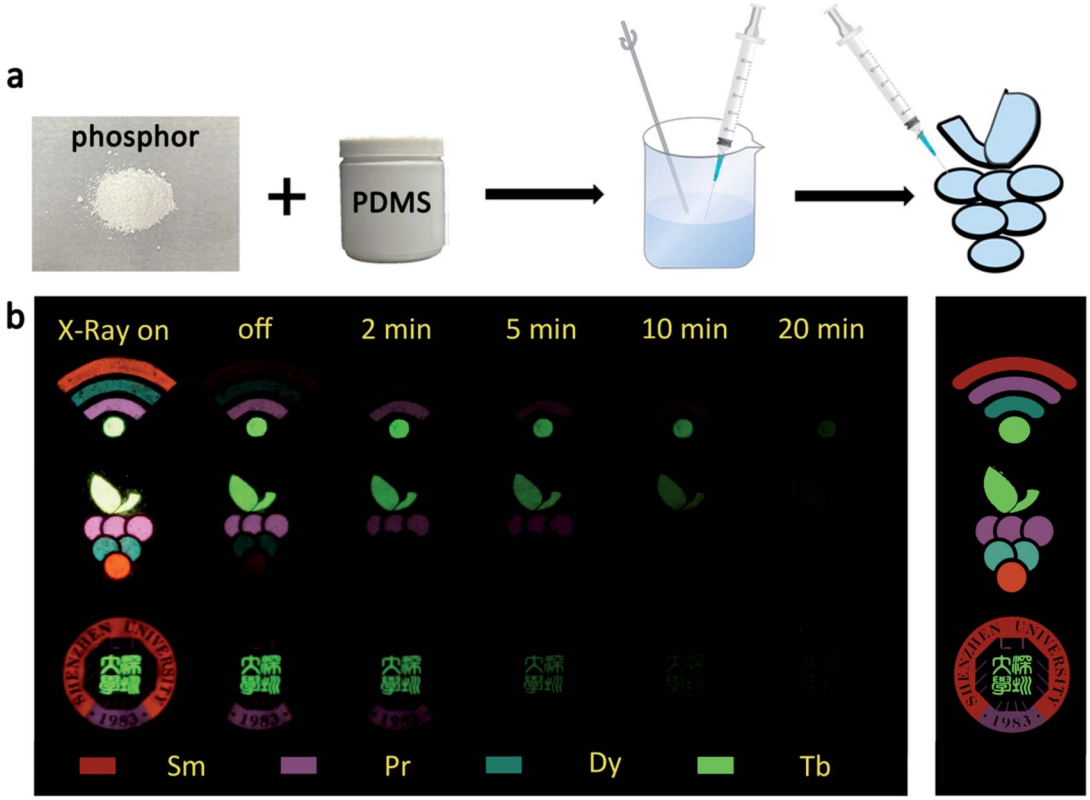

Fig. 6 (a) Fabrication process of the anti-counterfeiting patterns; (b) digital photos of the three designed patterns within a dynamic anti-counterfeiting process.

Conclusions

In summary, a series of β-$NaYF_4$:RE^{3+} (RE = Sm, Tb, Dy, Pr) PLPs were successfully fabricated using a simple hydrothermal method. These samples can be effectively activated by X-rays and can exhibit long lasting detectable afterglow signal even after 7 days. Persistent afterglow has been illustrated in terms of the trapping of electrons and holes by Frenkel defects ($V_F^{\bullet}$ and F_i') and the continuous recombination of them at Tb^{3+} centers. Based on the fact that the afterglow intensity is strongly correlated with decay time and dopant concentration, a dynamic anti-counterfeiting pattern was successfully fabricated by using the β-$NaYF_4$ PLPs with various Tb^{3+} doping concentrations. Furthermore, since the RL with the combined characteristics of multi-color emission and various afterglow time was achieved by Sm^{3+}, Tb^{3+}, Dy^{3+}, and Pr^{3+} doping, dynamic anti-counterfeiting patterns containing time-resolved multi-color information were successfully designed. We believe that our attempt on β-$NaYF_4$:RE^{3+} based dynamic anti-counterfeiting may effectively promote the development of the anti-counterfeiting field.

Experimental

Materials

The rare earth sources used for synthesis β-$NaYF_4$:RE^{3+} (RE = Sm, Tb, Dy, Pr) were $Sm(NO_3)_3 \cdot 6H_2O$ (99.99%), $Tb(NO_3)_3 \cdot 6H_2O$ (99.99%), $Dy(NO_3)_3 \cdot 6H_2O$ (99.99%), $Pr(NO_3)_3 \cdot 6H_2O$ (99.99%) and $Y(NO_3)_3 \cdot 6H_2O$ (99.99%), all purchased from Aladdin Industrial Inc. Shanghai, China. The other raw materials NaF (99.95%), NH_4F (99.9%), EDTA (99.9%) and HNO_3 (AR) were purchased from Sinopharm Chemical Reagent Co. Ltd. (Shanghai, China). All chemicals were used without further purification.

Synthesis of β-$NaYF_4$:RE^{3+} phosphor

β-$NaYF_4$:RE^{3+} crystals were produced through a conventional hydrothermal method. Briefly, certain amount of $Y(NO_3)_3 \cdot 6H_2O$ and $RE(NO_3)_3 \cdot 6H_2O$ (RE = Sm, Tb, Dy, Pr) were weighed and dissolved in deionized water. An aqueous solution containing EDTA (EDTA : RE^{3+} = 1 : 1) was then added to the above solution and stirred slowly for 30 min to get a homogeneous mixture. NaF and NH_4F (F^- : Na^+ : RE^{3+} = 8 : 1 : 1) were dissolved in deionized water and added dropwise into the above mixture, and pH of the obtained white suspension was adjusted to 5 by dilute HNO_3. After vigorous stirring for another 30 min, the final mixture was transferred into a stainless Teflon-lined autoclave. The autoclave was sealed tightly and maintained at 180 °C for 20 h, followed by naturally cooling to room temperature. The reaction products were collected by centrifugation and washed with ethanol for three times, then the β-$NaYF_4$:RE^{3+} PLPs were obtained after drying at 80 °C for 24 h.

Fabrication of the dynamic anti-counterfeiting patterns

A flexible thermoplastic polyurethane (TPU) model with shallow grooves was printed using a 3D printer. Then the PLPs and polydimethylsiloxane (PDMS, M_w = 22 000) were uniformly mixed by mass ratio of around 1 : 10, and the groove was filled with the obtained slurry. Finally, the model was heated at 60 °C for 5 h.

Characterizations

Powder X-ray diffraction (XRD) patterns of the samples were collected on a Rigaku Ultima IV X-ray diffractometer (Tokyo, Japan) using Cu Kα (λ = 0.15406 nm) radiation operated at 40 kV and 40 mA in a 2θ range from 10 to 70° with a step size of 0.02 at room temperature. The morphology of the samples was analysed by scanning electron microscope (SEM, Model APREO S, Thermo Scientific, Netherlands) operated under 1 kV. The elemental contents of the products were evaluated by energy disperse spectroscopy (EDS, Model APREO S, Thermo Scientific, Netherlands) for Na, Y, F and Tb. X-rays excited radio luminescence was measured using an X-ray tube (Model RACA-3, Zolix Instruments Co., Ltd, Beijing, China), controlled with a commercial software developed by Zolix. The spectra and the fluorescence decay curves were recorded by an Omni-λ 300i spectrograph (Zolix). The photoluminescence spectra were obtained using an FLS1000 fluorescence spectrograph (Edinburgh Instruments Ltd, UK), and a xenon lamp was used as the excitation source. The anti-counterfeiting pattern were taken with a SONY α7III camera, and the shooting parameters were Aperture: F4.0, shutter: 10 s, ISO: 4000.

Author contributions

Bohan Wang: conceptualization, methodology, material analysis, formal analysis, visualization, writing – original draft. Zhihao Wang: investigation, validation, material analysis, writing – review & editing. Peng Mao: material analysis. Yu Wang: conceptualization, funding acquisition, supervision, investigation, validation, project administration, writing – review & editing.

Conflicts of interest

There are no conflicts of interest to declare.

Acknowledgements

The work was supported by the Natural Science Foundation of China (Grant No. 61705137, 52002250), the Science and Technology Project of Shenzhen (KQJSCX20180328093614762). The authors acknowledge the assistance of the Instrumental Analysis Center of Shenzhen University (Lihu Campus) for SEM and EDS imaging.

References

1 H. Yang, W. Zhao, E. Song, R. Yun, H. Huang, J. Song, J. Zhong, H. Zhang, Z. Nie and Y. Li, *J. Mater. Chem. C*, 2020, **8**, 16533–16541.
2 S. Xie, G. Gong, Y. Song, H. Tan, C. Zhang, N. Li, Y. Zhang, L. Xu, J. Xu and J. Zheng, *Dalton Trans.*, 2019, **48**, 6971–6983.
3 Y. Hua and J. S. Yu, *Ceram. Int.*, 2021, **47**, 18003–18011.
4 X. Fan, J. Nie, W. Ying, S. Xu, J. Gu and S. Liu, *Dalton Trans.*, 2021, **50**, 12234–12241.
5 B. Song, H. Wang, Y. Zhong, B. Chu, Y. Su and Y. He, *Nanoscale*, 2018, **10**, 1617–1621.
6 J. Li, D. Xia, M. Gao, L. Jiang, S. Zhao and G. Li, *Inorg. Chim. Acta*, 2021, **526**, 120541.
7 T. Si, Q. Zhu, J. Xiahou, X. Sun and J. G. Li, *ACS Appl. Electron. Mater.*, 2021, **3**, 2005–2016.
8 X. Chen, J. Song, X. Chen and H. Yang, *Chem. Soc. Rev.*, 2019, **48**, 3073–3101.
9 Z. Zeng, B. Huang, X. Wang, L. Lu, Q. Lu, M. Sun, T. Wu, T. Ma, J. Xu, Y. Xu, S. Wang, Y. Du and C. H. Yan, *Adv. Mater.*, 2020, **32**, 1–10.
10 J. Liu, Y. Liang, S. Yan, D. Chen, S. Miao, W. Wang and J. Bi, *J. Mater. Chem. C*, 2021, **9**, 9692–9701.
11 Y. Zhang, D. Chen, W. Wang, S. Yan, J. Liu and Y. Liang, *Inorg. Chem. Front.*, 2020, **7**, 3063–3071.
12 A. Abdukayum, J. T. Chen, Q. Zhao and X. P. Yan, *J. Am. Chem. Soc.*, 2013, **135**, 14125–14133.
13 A. Bessière, S. Jacquart, K. Priolkar, A. Lecointre, B. Viana and D. Gourier, *Opt. Express*, 2011, **19**, 10131.
14 N. Yu, F. Liu, X. Li and Z. Pan, *Appl. Phys. Lett.*, 2009, **95**, 231110.
15 J. Du and D. Poelman, *J. Phys. Chem. C*, 2020, **124**, 16586–16595.
16 D. Kim, *Nanomaterials*, 2021, **11**, 1–27.
17 Z. Yi, Z. Luo, N. D. Barth, X. Meng, H. Liu, W. Bu, A. All, M. Vendrell and X. Liu, *Adv. Mater.*, 2019, **31**, 1–7.
18 C. Liu, H. Wang, X. Li and D. Chen, *J. Mater. Chem.*, 2009, **19**, 3546–3553.
19 L. Wang and Y. Li, *Chem. Mater.*, 2007, **19**, 727–734.
20 Q. Shao, H. Zhang, J. Dai, C. Yang, X. Chen, G. Feng and S. Zhou, *CrystEngComm*, 2019, **21**, 741–748.
21 Q. Wang, Y. Liu, B. Liu, Z. Chai, G. Xu, S. Yu and J. Zhang, *CrystEngComm*, 2013, **15**, 8262–8272.
22 X. Ou, X. Qin, B. Huang, J. Zan, Q. Wu, Z. Hong, L. Xie, H. Bian, Z. Yi, X. Chen, Y. Wu, X. Song, J. Li, Q. Chen, H. Yang and X. Liu, *Nature*, 2021, **590**, 410–415.
23 Y. Hu, Y. Yang, X. Zhang, X. Wang, X. Li, Y. Li, T. Li and H. Zhang, *J. Phys. Chem. C*, 2020, **124**, 24940–24948.
24 A. B. Bard, X. Zhou, X. Xia, G. Zhu, M. B. Lim, S. M. Kim, M. C. Johnson, J. M. Kollman, M. A. Marcus, S. R. Spurgeon, D. E. Perea, A. Devaraj, J. Chun, J. J. De Yoreo and P. J. Pauzauskie, *Chem. Mater.*, 2020, **32**, 2753–2763.
25 M. Wang, H. Wu, W. Dong, J. Lian, W. Wang, J. Zhou and J. Zhang, *Inorg. Chem.*, 2022, **61**, 2911–2919.
26 A. Aebischer, M. Hostettler, J. Hauser, K. Krämer, T. Weber, H. U. Güdel and H. B. Bürgi, *Angew. Chem., Int. Ed.*, 2006, **45**, 2802–2806.

27 D. Yang, Z. Peng, X. Guo, S. Qiao, P. Zhao, Q. Zhan, J. Qiu, Z. Yang and G. Dong, *Adv. Opt. Mater.*, 2021, **9**, 1–10.
28 C. Renero-Lecuna, R. Martín-Rodríguez, R. Valiente, J. González, F. Rodríguez, K. W. Krämer and H. U. Güdel, *Chem. Mater.*, 2011, **23**, 3442–3448.
29 J. H. Burns, *Inorg. Chem.*, 1965, **4**, 881–886.
30 P. Chen, M. Song, E. Wu, B. Wu, J. Zhou, H. Zeng, X. Liu and J. Qiu, *Nanoscale*, 2015, **7**, 6462–6466.
31 X. Sun, X. Wang, B. Chen, F. Zhao, X. Xun, K. Ren, Y. Lu, X. Qiao, G. Qiao and X. Fan, *CrystEngComm*, 2019, **21**, 6652–6658.
32 N. Bogdan, F. Vetrone, G. A. Ozin and J. A. Capobianco, *Nano Lett.*, 2011, **11**, 835–840.
33 X. Li, Z. Xue, M. Jiang, Y. Li, S. Zeng and H. Liu, *Nanoscale*, 2018, **10**, 342–350.
34 W. Wang, Z. Sun, X. He, Y. Wei, Z. Zou, J. Zhang, Z. Wang, Z. Zhang and Y. Wang, *J. Mater. Chem. C*, 2017, **5**, 4310–4318.
35 C. Wang, Y. Jin, Y. Lv, G. Ju, D. Liu, L. Chen, Z. Li and Y. Hu, *J. Mater. Chem. C*, 2018, **6**, 6058–6067.
36 R. Chen, *J. Appl. Phys.*, 1969, **40**, 570–585.
37 L. C. V. Rodrigues, H. F. Brito, J. Hölsä, R. Stefani, M. C. F. C. Felinto, M. Lastusaari, T. Laamanen and L. A. O. Nunes, *J. Phys. Chem. C*, 2012, **116**, 11232–11240.
38 P. Dorenbos and A. J. J. Bos, *Radiat. Meas.*, 2008, **43**, 139–145.
39 P. Dorenbos, *J. Phys. Condens. Matter*, 2003, **15**, 8417–8434.
40 X. Liu, Q. Ji, Q. Hu, C. Li, M. Chen, J. Sun, Y. Wang, Q. Sun and B. Geng, *ACS Appl. Mater. Interfaces*, 2019, **11**, 30146–30153.
41 Y. Zhuang, D. Chen, W. Chen, W. Zhang, X. Su, R. Deng, H. Chen and R. Xie, *Light Sci. Appl.*, 2021, **10**, 1–10.
42 J. Dong, Y. Liu, J. Yang, H. Wu, C. Yang and S. Gan, *J. Lumin.*, 2019, **207**, 397–407.
43 Z. Smara, Y. Cheroura, D. Boyer, A. Potdevin, A. Chafa, O. Ziane and R. Mahiou, *Opt. Mater.*, 2020, **104**, 109932.
44 B. Liu, W. Chen and S. Jin, *Organometallics*, 2007, **26**, 3660–3667.
45 L. Ji, J. Zhou, J. Zhang, Z. Zhang, Z. Ma, W. Wang, H. Li and C. Wu, *J. Am. Ceram. Soc.*, 2019, **102**, 5465–5470.
46 T. J. de Prinse, A. Karami, J. E. Moffatt, T. B. Payten, G. Tsiminis, L. D. S. Teixeira, J. Bi, T. W. Kee, E. Klantsataya, C. J. Sumby and N. A. Spooner, *Adv. Opt. Mater.*, 2021, **9**, 1–7.
47 R. Hu, Y. Zhang, Y. Zhao, X. Wang, G. Li and C. Wang, *Chem. Eng. J.*, 2020, **392**, 124807.
48 W. Dong, W. Wang, M. Wang, J. Zhang and Y. Wang, *J. Mater. Chem. C*, 2022, **10**, 4218–4223.